Journal of
Mechanics of
Materials and Structures

FACTORS THAT INFLUENCE THE LATERAL CONTACT FORCES IN BUCKLING-RESTRAINED BRACES: ANALYTICAL ESTIMATES

Francesco Genna

Volume 15, No. 3 May 2020

msp

JOURNAL OF MECHANICS OF MATERIALS AND STRUCTURES
Vol. 15, No. 3, 2020
https://doi.org/10.2140/jomms.2020.15.379

FACTORS THAT INFLUENCE THE LATERAL CONTACT FORCES IN BUCKLING-RESTRAINED BRACES: ANALYTICAL ESTIMATES

FRANCESCO GENNA

Dedicated to the memory of Laura Da Lisca

An analytical technique for the calculation of the lateral contact forces in buckling-restrained braces (BRBs), proposed by Dehghani and Tremblay (2017), is critically revised and improved. The resulting algorithm is implemented and adopted with the only aim of highlighting what factors are important in the calculation of the lateral thrust in BRBs. Many of these factors seem to have a marginal importance in comparison with the buckled shape of the core, the core steel constitutive law, and the stiffness of the retention profiles. Possible conclusions deriving from this analysis are (i) only the calculation of analytical upper and lower limits for the lateral thrust in BRBs may have a sense, but these limits are always much distant from each other, and (ii) it is worthless trying to adopt over-detailed calculation techniques for this important quantity.

1. Introduction

Buckling-restrained braces (BRBs), designed to dissipate energy also in compression through the limitation of the elastic-plastic buckling amplitude of a steel core, are increasingly adopted in engineering practice. Their design is based on commonly accepted procedures, aimed at preventing their global buckling, failures due to plastic collapse/fatigue, and failures of the end connection (or other) details. There is not space here for a review of this topic and of the abundant literature concerning it. Useful information could be obtained, for example, from [Takeuchi and Wada 2017].

In spite of this situation, a main engineering quantity, in BRBs, still seems to remain very difficult to be accurately calculated. This quantity is the lateral contact force, or thrust, generated by the buckled core when reaching contact against the external retention profiles. These forces, at each contact point, have both a normal and a tangential component. The retention profiles should be designed on the basis of the values of these contact forces. If the normal contact forces become too high, there is the risk, for example in the case of bolted all-steel BRBs, of an explosive failure of the bolts.

Yet the determination of the lateral contact forces in any BRB is very problematic, which makes problematic also the correct design of the retention profiles. Strangely, there seems to be very little published work on the experimental side of this specific aspect. Almost the totality of the attention has been devoted to the BRB hysteretic (axial) behavior only. Besides the references quoted in the sequel of this work, to this author's knowledge only [Dehghani and Tremblay 2018] provides some information of the experimental type about the lateral thrust in BRBs; [Dehghani and Tremblay 2017; Jiang et al. 2015] also devote some attention to this aspect, but through numerical analyses only.

Keywords: buckling-restrained braces, contact forces, analytical methods.

In this work the term "total lateral thrust", denoted by the symbol Q_{TOT}, indicates the sum of all the contact normal forces at one side of the BRB core. The value of Q_{TOT} depends on many factors, some of which are difficult to properly take into account. The main one is the shape and the number of the core buckled waves. It was shown in [Genna and Bregoli 2014] that, given a value of the axial shortening of the BRB core beyond its first buckling limit, both the number of buckled waves and the wave shape are not uniquely defined, but that several buckled configurations exist, all equally possible. Finite element (FEM) analyses [Genna 2019] have shown that the computed value of the total lateral thrust is extremely sensitive to any modeling detail. Different FEM models may produce, for the same BRB problem, values of Q_{TOT} differing from each other by a factor of almost 3. In [Genna 2020], it was shown experimentally that the measured values of Q_{TOT}, in 11 nominally identical BRB samples, varied in a range one order of magnitude wider than the range of the experimentally measured axial forces. The minimum value measured of Q_{TOT} was one half of the maximum one.

Even having full control over all the other important factors — which is not the case anyway — the multiplicity of possible buckled configurations alone makes it impossible to predict with an acceptable engineering accuracy the value of the total lateral thrust in BRBs. The configuration "chosen" by a buckled BRB core, especially after a sequence of tensile-compressive loading cycles, depends essentially on the existing imperfections. No engineer has enough control over the imperfections to enable a sensible choice between multiple solutions associated with quite different values of structural forces.

This complication appears to be inherent in any BRB design type. In fact, every BRB, by its very nature, comprises a yielding segment which undergoes a multiwave plastic buckling under shortening. This phenomenon is the essence of any BRB properly functioning; there is no way to avoid it, or stay clear from it, as happens for example when dealing with ordinary compressed structural elements. In these, it is normal practice to stay well below the theoretical buckling limit so as to reduce to a minimum the sensitivity of the response to the imperfections. But in an element designed to work exploiting buckling this sensitivity always exists, and dominates the response, at least in some of its aspects. The axial force in BRBs, for example, is not sensitive to the imperfections, precisely because the buckled amplitude is limited; but the lateral thrust Q_{TOT} definitely is, as clearly shown in [Genna 2019; 2020].

Workarounds to this unfortunate situation seem to be of two types. A first one is to resort to extensive preliminary experimental verifications of each new BRB design, so as to have significant statistics, covering a large enough variety of imperfections, providing an engineering sufficient guarantee of the structural safety. This obviously is a very expensive procedure, and not ordinary engineering practice.

Another possibility could be to compute a theoretical range of values for the total lateral thrust, and selecting some value high enough to allow a safe design procedure. To this purpose, analytical tools could be adopted.

Several attempts have been made to produce analytical techniques for the calculation of the lateral thrust in BRBs. Many of these techniques, however, appear to be based on wrong assumptions, among which the main one is of adopting Euler's relationship between the compressive axial load and the buckled wavelength. It was proved first in [Genna and Gelfi 2012], and later in [Genna and Bregoli 2014], that, owing to the existence of contact, this is not the case, by a large amount.

One of the most refined analytical techniques is proposed in [Dehghani and Tremblay 2017], where many aspects of the problem are taken into account. This technique appears correct in its main essence, but seems to give even too much attention to details which may be of little or no importance with respect

to the tremendous uncertainty introduced by the selection of the shape and number of buckled waves. In the present work the technique of Dehghani and Tremblay [2017] is taken as a starting point. An attempt is made at improving some aspects and possibly rectifying some imprecisions. Several engineering and modeling factors are taken explicitly into account, and can be controlled.

This analytical tool is adopted here with the only aim of understanding which are the important factors for the calculation of the total lateral thrust, and which are inessential. No comparison with "real" results, either experimental or FEM, is made. If interested, the reader may find some experimental and/or numerical results, to be compared with the analytical ones of Section 4 later on, in [Bregoli et al. 2016; Genna 2019; Metelli et al. 2016; Dehghani and Tremblay 2018; 2017].

The results illustrated here may help in allowing one to eventually produce the simplest possible analytical tool yet able to provide an acceptable range of values (a single "exact" one does not exist, as explained here above) for the lateral thrust in a given BRB. It will remain a (difficult anyway) decision of engineers how to select, in the computed range, the most appropriate lateral thrust value, to be adopted for the correct design of the retention profiles.

2. Considered BRB model and general assumptions

Reference is made to the BRB model shown in Figure 1. The top image shows a dissipative core, of length L, with a rectangular cross-section of height t and width b, placed between two restraining profiles whose global elastic stiffness, including possible connection elements such as bolts, is denoted by K_{TOT} (dimension of force/displacement) at each side of the core. At the top and the bottom of the core a free gap exists of width equal to $g/2$. It is assumed, with no loss of generality, that the core is connected to the restraining profiles at the center point, where therefore no relative slip can occur. This point is indicated as *FP* (fixed point). The core is assumed to be made of an elastic-plastic hardening material, and the restraining profiles are assumed to behave elastically.

The image below shows a sketch of the BRB buckled configuration under an adequate axial shortening, associated to horizontal compressive forces H_{END} at the core ends. From here on, reference will be made to horizontal and vertical force components always assuming that the axis of the undeformed core is horizontal. At each contact point, between core and restraining profiles, both normal and tangential forces develop. The tangential forces, due to friction, cause a jump in the horizontal internal force at each contact point, thus causing several jumps of the horizontal forces in each half-wave. This, in turn, produces an increase in the normal contact forces moving away from the *FP*; this is the reason for the sketched increase of the retention profiles opening in the central image of Figure 1.

It has to be remarked that the reality might be different, in dependence on the local stiffness details of the restraining profiles (for example, connection bolts). These can cause smaller openings at the core ends rather than at its mid-zone. In the present work, however, no local stiffness detail of the restraining profiles will be taken into consideration.

In the configuration shown in Figure 1, the relative slip between core and retention profiles occurs from the ends of the core towards the *FP*; therefore, all the tangential contact forces are directed to the left in the left part of the core, and to the right in the right part.

The bottom images in Figure 1 depict a single buckled wave and illustrate the adopted mechanical scheme. In this, at each contact zone the local stiffness provided by the retention profiles is approximated

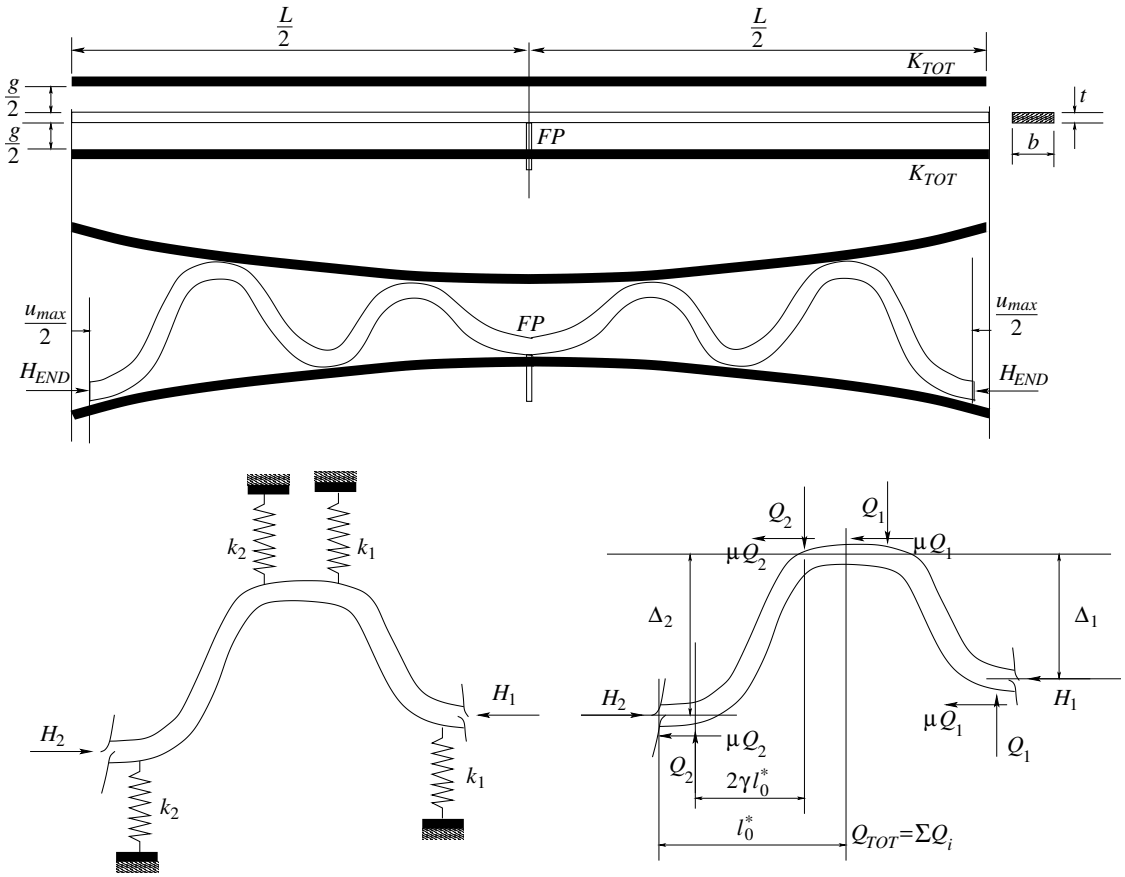

Figure 1. Top: BRB scheme. Center: BRB buckled shape under axial shortening. Bottom: detail of a core buckled wave, taken from the left side of the BRB, where the relative slip between core and restraining profiles occurs towards the left.

by two linear elastic springs. The core buckled half-wave length is denoted by l_0 with reference to the undeformed configuration, and by l_0^* on the deformed configuration (more details about this later on). The symbol γ, in the right bottom image, defines the central portion of a buckled half-wave which joins two contact points at the opposite sides of the core, so that the length of this portion, denoted by l_B, is equal to

$$l_B = 2\gamma l_0. \tag{1}$$

The other symbols adopted in the right bottom image refer to the horizontal internal forces H_i, existing in the various portions of the core, and to the contact forces. The normal contact forces at each contact point are denoted by Q_i. A Coulomb friction model is assumed, governed by a friction coefficient μ, which provides a maximum possible value, for the tangential forces, equal to μQ_i at each contact point. The total lateral thrust Q_{TOT} is the sum of all the normal contact forces Q_i at one side of the core:

$$Q_{TOT} = \sum_{i=1}^{C} Q_i \tag{2}$$

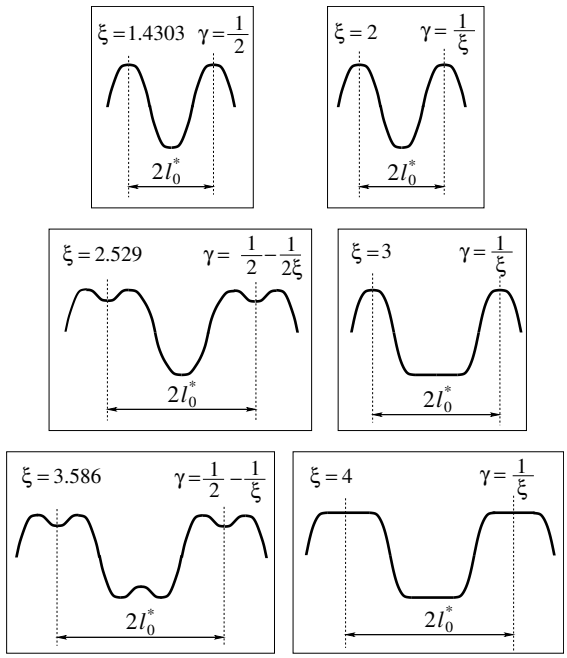

Figure 2. Possible buckled shapes of BRB cores, according to [Genna and Bregoli 2014]. The indicated values of parameters ξ and γ are valid only for sufficiently stiff restraining profiles.

where C denotes the total number of contact points at each side of the core. This is the main quantity of interest in the present work.

The main difficulty, in this problem, is the determination of the buckled half-wave length l_0 associated to a given value of the horizontal load in the core. This issue was first tackled in [Genna and Bregoli 2014], where a much simplified situation was studied, but it was nevertheless found that at least 6 possible buckled configurations can exist under the same horizontal load. For each of these configurations a specific corresponding value of the horizontal force could be obtained. A convenient way for expressing this relationship is the following one, for the moment ((11) will be adopted later on for the elastic-plastic case) associated to a purely elastic buckling of the BRB core:

$$l_0 = \xi \pi \sqrt{\frac{EI}{H}} \tag{3}$$

where E is the Young modulus of the material, I is the weak-axis moment of inertia of the core cross-section (here $I = bt^3/12$), H is the horizontal internal force associated to the buckled half-wavelength, and ξ is a parameter that depends on the shape of the buckled wave. Equation (3), for $\xi = 1$, provides the familiar Euler buckling load. Owing to the existence of the restraining profiles, for this problem the value of ξ can take values much higher than $\xi = 1$. To each possible value of ξ, a unique value of γ of (1) is associated.

Figure 2 illustrates the 6 possible buckled configurations, for one buckled wave, individuated in [Genna and Bregoli 2014], together with the corresponding values for the parameters ξ and γ. In this figure, for

simplicity, it is assumed that two adjacent half-waves have the same length l_0^* in the deformed configuration. This happens only if the contact between core and restraining profiles is frictionless. The indicated numerical values for the parameter ξ are rigorously valid only for the limiting case of rigid restraining profiles. Nevertheless, the normal stiffness of the restraining profiles is high enough to allow the formation of these buckled configuration for the indicated values of ξ. The difference between the top two cases is associated to their development under an increasing core shortening: for $\xi = 1.4303$ a point contact remains, and for $\xi = 2$ a flat line contact starts developing.

From the theoretical viewpoint no situation, among the 6 illustrated in Figure 2, is to be preferred. This leaves open the choice of a wide range of values for ξ (even wider if the restrainers have an insufficient stiffness). Notice that, given a value of l_0, for $\xi = 2$ the corresponding horizontal force is 4 times larger than Euler's one, according to (3), and for $\xi = 4$ it is 16 times larger than Euler's load. Therefore, the definition of parameter ξ is a crucial point in this calculation.

In setting up the equations for computing the Q_i values, and their resultant Q_{TOT}, the following main assumptions will be made.

(a) The studied BRB model is supposed, for simplicity, to be subjected to tensile and compressive cycles of the same amplitude, defined by the peak value of the average strain ε_0:

$$\varepsilon_0 = \frac{u_{max}}{L}, \tag{4}$$

u denoting the horizontal displacement of the core ends, and u_{max} its peak value. A generalization to unsymmetric cycles is easy to consider.

(b) The bending moment at the contact points is always considered equal to zero. This allows one to greatly simplify the problem, and is in fact a crucial assumption, taken also in [Dehghani and Tremblay 2017], to obtain a technique which solves the problem one half-wave at a time. In reality, if a line contact develops the bending moment is rigorously equal to zero in all the contact zones; but if a point contact develops this may not be the case.

(c) The fixed point *FP*, assumed to be at the mid-point of the core as in Figure 1, is supposed to be in contact with one restraining profile, and the buckled configuration is assumed to be symmetric with respect to the *FP*. This assumption is somewhat limiting, since it is known, from both experiments and numerical simulations, that the buckled configuration, even considering it made by identical half-waves, can be associated to a rigid rotation of the core, so that the contact points, at the two core ends, can be at the opposite sides of the core, with an odd total number of half-waves [Bregoli et al. 2016].

(d) The adopted stress-strain equation for the steel core is the uniaxial one of Ramberg and Osgood [1943]:

$$\sigma = \frac{E\varepsilon}{1 + \alpha(|\sigma|/\sigma_0)^{n-1}} \tag{5}$$

where σ_0 is the yield stress, and α and n are material parameters.

(e) The local tangential contact forces due to the friction, at each contact point, will usually be considered equal to their maximum value, i.e., μQ_i if Q_i is the value of the local normal contact force at that point. This assumption is correct if a continuous slip occurs between core and restraining profiles after contact

is reached. Nevertheless, preliminary experimental results shown in [Genna 2020] indicate that this may not always be the case. A part of the results shown in Section 4 will explore the importance of this aspect.

(f) In order to adapt (3) to the elastic-plastic case, an approach similar to the one taken in [Bregoli et al. 2016], accounting also for later observations [Dehghani and Tremblay 2017; Genna 2020], is followed.

In the first place, to account for the assumed cyclic loading type, the value of the horizontal load in (3) is redefined following what was proposed in [Bregoli et al. 2016] but accounting for a nonlinear stress-strain constitutive law:

$$H_{cic} = \sigma_{cic} A, \quad \sigma_{cic} = \sigma(\varepsilon_{cic}), \quad \varepsilon_{cic} = \left(2\varepsilon - \frac{\sigma_0}{E}\right) \tag{6}$$

where ε indicates the actual value of the average core strain in the considered configuration and in the considered point. This replaces (9) of [Dehghani and Tremblay 2017].

Next, in (3) the Young modulus E should be replaced by a different modulus, that takes into account the reduced stiffness existing in the plastic range. In [Genna and Gelfi 2012], use of Shanley's theory was made, replacing the value of E with the value of a tangent modulus E_t. Dehghani and Tremblay [2017] have adopted an "effective modulus", intermediate between the elastic and the tangent one (their (1)). They proposed an empirical nonlinear model both for the stress-strain equation and for their "effective modulus". In the present work a third approach is followed, based on recent results to be found in [Genna 2020], both experimental and numerical. According to these results, for this BRB problem the formation of a new buckled wave occurs with plastic loading in the compressed portion of the core cross-section, and elastic unloading in the portion elongated due to the bending. This suggests the adoption of the reduced modulus E_R of the von Kármán theory of elastic-plastic buckling (see for example [Bažant and Cedolin 1991]). Accordingly, in the present work the adopted material modulus for the expression of the buckled half-wave length will be

$$E_R = \left[\frac{1}{2}\left(\frac{1}{\sqrt{E}} + \frac{1}{\sqrt{E_t}}\right)\right]^{-2} \tag{7}$$

valid for a rectangular cross-section [Bažant and Cedolin 1991], and where E_t is the local tangent modulus provided by (5) at a strain equal to ε_{cic} of (6), i.e.,

$$E_t = E\left[\alpha n\left(\frac{\sigma_{cic}}{\sigma_0}\right)^{n-1} + 1\right]^{-1}. \tag{8}$$

Finally, it may be of importance to replace the standard value of the moment of inertia I of (3) with one corrected to take into account the effect of both the elastic Poisson effect and the plastic incompressibility (here we introduce another difference with respect to [Dehghani and Tremblay 2017]). For a given average compressive axial strain ε, at some point along the core axis, these effects produce a transversal strain ε_t, here associated to widening of both the core sides, equal to

$$|\varepsilon_t| = \tfrac{1}{2}\varepsilon + \frac{\sigma}{E}\left(\nu - \tfrac{1}{2}\right), \tag{9}$$

ν being the elastic Poisson coefficient. As a consequence, the modified cross-section moment of inertia is given by

$$I^* = \tfrac{1}{12} b t^3 (1 + c_\nu |\varepsilon_t|)^4. \tag{10}$$

The coefficient c_v, to be set equal to 0 or 1, is inserted to enable the evaluation of the importance of this effect.

In conclusion, the expression adopted to relate the value of the horizontal force to the buckled half-wave length is

$$l_0 = \xi\pi\sqrt{\frac{E_R I^*}{H_{cic}}}. \tag{11}$$

(g) A constant value for the parameter ξ in (11), chosen among the 6 possible of Figure 2, is considered along all the buckled core, implying that all the buckled half-waves have the same shape. In reality this is not guaranteed to happen: waves of different shapes, along one BRB core, are often observed in both experimental and numerical results. This phenomenon is a further big complication, due to the sensitivity to imperfections, and very difficult, if not impossible, to be properly taken into account in a theory.

Moreover, and unlike what was done previously for example in [Bregoli et al. 2016], the value for ξ has been considered as a datum, one of the 6 values of Figure 2. In [Bregoli et al. 2016], the periodicity of the buckled shape was assumed for simplicity, and also only an integer number of equal half-waves was always considered, assuming that both the extreme points of the core were at contact with the restraining profiles. To account for this situation, in [Bregoli et al. 2016], the final value of ξ had to be adjusted, starting anyway from one of those indicated in Figure 2, so as to produce a value of l_0 associated to an integer number of half-waves. If ξ is considered as unknown, however, the adopted solution technique to compute Q_{TOT} would become much more complicated, requiring the solution of the problem for the full BRB core instead of solving one half-wave at a time. Therefore, and considering also that the value of l_0 in reality changes at each half-wave because of friction, it was decided here to keep the chosen value of ξ fixed for all the half-waves except the last (core ends) one, as explained in the next section.

(h) No account is taken of a possible strong-axis buckling of the core or of other out-of-plane effects. Strong-axis buckling may happen in reality (limited anyway by the restraining profiles, and with just one wave), but it does not seem to influence the main weak-axis behavior [Genna 2019].

(i) No account is taken of the important dependence of the lateral thrust on the number of loading cycles, even when they are of the same amplitude. As shown experimentally [Metelli et al. 2016], at each new cycle of the same amplitude, at least for the first cycles, the lateral thrust increases significantly, up to 100%, owing to a progressive "flattening" of the core portions in contact with the restraining profiles. Accounting for this phenomenon analytically seems for the moment out of the question. It must be noted that this phenomenon can be found numerically using a standard hardening model with no dependence on the cycle number. Therefore, the adoption of a stress-strain equation including a dependence on the cycle number, as done in [Dehghani and Tremblay 2017], is not crucial to obtain this effect. This is a further reason to choose the simple Ramberg–Osgood constitutive model of (5), which requires the definition of just 3 plastic material parameters.

Further specific details on the modeling technique are given in the next section.

3. Solution technique

The main purpose of the model described in the previous section is the calculation of the lateral thrust Q_{TOT} associated to a given set of data, including a prescribed end displacement maximum amplitude u_{max}. The

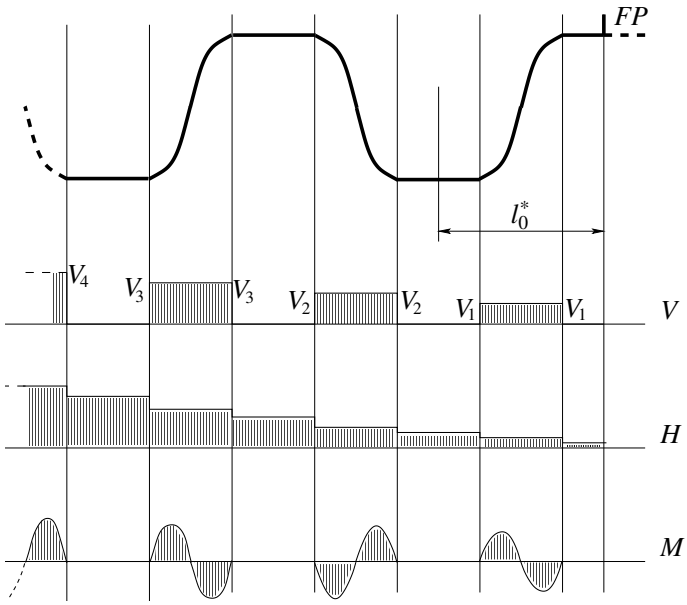

Figure 3. Considered buckled shape for the analytical developments (symmetric line contact). The diagram marked by a V shows the internal vertical force along the buckled core; the one marked by N shows the internal horizontal force along the core; the bottom one, marked by M, shows the bending moment along the core. In the frictionless case, the values of V remain constant, i.e., $V_1 = V_2 = V_3 =$, etc., and also the force H has no jumps along the core. Likewise, in the frictionless case the bending moment diagrams in the inclined portions of the core are the same for all the waves.

approach followed is based on the one described in [Dehghani and Tremblay 2017]. The calculation proceeds one half-wave at a time, accounting for the variation of both the internal forces and the associated half-wave lengths due to the friction. Beside what already illustrated in the previous section, however, other modifications have been introduced, as explained next.

3.1. ***Governing equations.*** Figure 3 sketches the considered geometry of the buckled core and the associated evolution of the internal forces. V is the vertical internal force, i.e., the shear force in the flat core portions. V is considered positive if it gives a positive contribution to the lateral thrust. H is the horizontal internal force, i.e., the axial force in the flat core portions, considered positive if compressive; and M is the bending moment. In the core portion of Figure 3, the motion occurs towards the right, and the contact tangential forces are all directed towards the left; this is the reason for the increase of the internal forces proceeding from the FP towards the left.

In Figure 3, as well as in all the analytical calculations, a symmetric line contact configuration has been assumed as the basic buckled configuration. This is convenient because it allows one to treat the local contact forces as split into two concentrated parts, located at the two extreme points of the flat contacting portions of the core. This is reflected in the assumed plot of the internal vertical forces V of the figure. In this way, unlike the case of single point contact configurations, the equilibrium equations for a single half-wave involve only quantities defined on that half-wave.

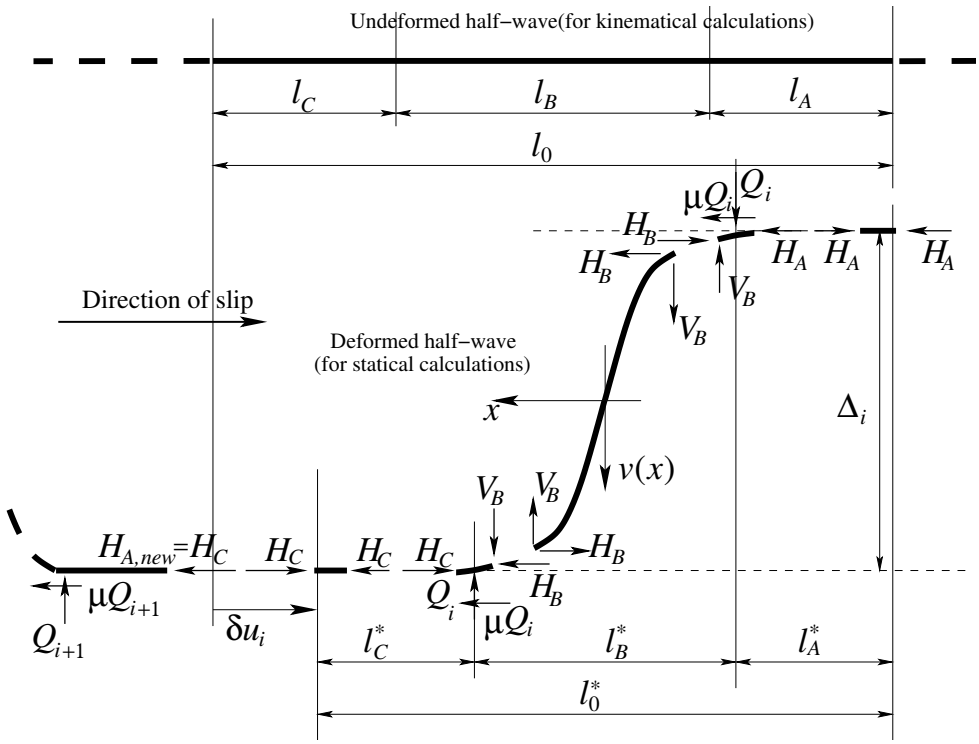

Figure 4. Undeformed (top) and deformed (bottom) shape of a generic half-wave of the buckled core. H denotes horizontal internal forces; V denotes internal vertical forces; Q denotes a local normal contact force. μ is the friction coefficient. All the other symbols are explained in the text.

Since the results of Section 4 will consider also values of ξ related to point contact configurations, for these cases it will be assumed that the single contact point configuration is the limiting case, with zero length, of a line contact configuration, so that the equilibrium equations, as described next, remain still valid.

Figure 4 shows all the forces — external and internal — considered on a single generic half-wave. The top image refers to the undeformed — horizontal — shape, where l_0, given by (11), is the half-wave length, and l_A, l_B, and l_C denote the three portions of the half-wave. l_B is the length of the central part, inclined in the deformed configuration, defined by the parameter γ as in (1).

The lengths of the 2 lateral flat portions are assumed, with no loss of accuracy even for the cases in which they are not, to be equal:

$$l_A = l_C = \tfrac{1}{2}(l_0 - l_B) = \frac{1-2\gamma}{2} l_0 \tag{12}$$

(see (1)). These quantities will be adopted for all the calculations involving the kinematics of this problem, which is treated in a second-order theory, i.e., as infinitesimal. Equilibrium is instead defined on the deformed configuration, shown in the bottom part of Figure 4.

The half-wave axis line has undergone a bending limited by the restraining springs. The vertical distance between the core axes at the top and the bottom points of the central part, denoted as Δ_i in Figure 4, can be expressed as

$$\Delta_i = g + c_{spr}\frac{2Q_i}{k_i} - c_\nu t \varepsilon_{tB}. \tag{13}$$

Here, g is the initial total gap between core and restraining profiles; the second addend derives from the elastic opening of the restraining profiles; the last term accounts for both the Poisson and the plastic incompressibility effects, as was done in (10). In this term, the lateral strain ε_{tB} is the one existing in the inclined portion of the core, given by (9). The local spring stiffness k_i is determined as

$$k_i = \frac{K_{TOT} l_0}{L} \tag{14}$$

(recall that two springs are introduced at each contact line, as in Figure 1, each of stiffness k_i). The coefficients c_{spr} and c_ν, in (13), enable the evaluation of the importance of the associated terms. If $c_{spr} = 0$ the restraining profiles are treated as rigid. If $c_\nu = 0$ the Poisson + plastic incompressibility effects are neglected.

The horizontal shortening δu_i of the considered half-wave is the sum of two terms, an axial one, associated to the average strains, and a bending one, denoted by u_B, as

$$\delta u_i = (\varepsilon_A l_A + \varepsilon_B l_B + \varepsilon_C l_C) + c_{ub} u_B, \tag{15}$$

in which a coefficient c_{ub} has been inserted to enable the evaluation of the importance of the bending contribution to the axial shortening.

In all the equations adopted in this work, compression and shortening are always considered positive.

The value for the contribution u_B, denoting by $v(x)$ the bending deflection function in the central portion of the half-wave (see Figure 4), can be evaluated, in a second-order theory, by the standard expression

$$u_B = \frac{1}{2}\int_{-\gamma l_0}^{\gamma l_0} v'^2(x)\, dx. \tag{16}$$

The function $v(x)$ can be approximated as

$$v(x) = \frac{\Delta_i}{2}\sin\frac{2\pi x}{4\gamma l_0}. \tag{17}$$

Inserting (17) into (16) one obtains

$$u_B = \frac{\pi^2 \Delta_i^2}{32\gamma l_0}, \tag{18}$$

different from (8) of [Dehghani and Tremblay 2017].

Equilibrium is governed by the following equations:

$$V_B = Q_i, \tag{19}$$

vertical translation of the top small portion of core subjected to the local contact forces;

$$H_B = H_A + \mu Q_i, \tag{20}$$

horizontal translation of the top small portion of core subjected to the local contact forces;

$$H_C = H_B + \mu Q_i = H_A + 2\mu Q_i, \tag{21}$$

horizontal translation of the bottom small portion of core subjected to the local contact forces; and

$$H_B \Delta_i = V_B l_B^* = Q_i l_B^*, \tag{22}$$

rotation of the inclined segment of core. In this equation use was made of the deformed length l_B^*, which can be obtained, on the basis of Figure 4, as

$$l_B^* = l_B - c_{l*}(l_B \varepsilon_B + u_B). \tag{23}$$

Once again, a coefficient c_{l*} was inserted to enable the evaluation of the importance of the difference between l_B and l_B^* in these calculations.

These equations are different from the simpler ones adopted in [Dehghani and Tremblay 2017]. There, in fact, the horizontal forces have been considered constant in the whole half-wave, ignoring the jumps due to the tangential frictional forces between the flat and the inclined portions of the half-wave.

Finally, the relationships between stresses and forces are

$$H_A = \sigma_A A_A^*, \quad H_B = \sigma_B A_B^*, \quad H_{B,cic} = \sigma_{B,cic} A_B^*, \quad H_C = \sigma_C A_C^*. \tag{24}$$

Here, the starred quantities, for the cross-section areas A_n, account for the core lateral expansion due to the combined Poisson and plastic incompressibility effects, and are computed as

$$A_n^* = A_n(1 + c_\nu |\varepsilon_{n,t}|)^2 \tag{25}$$

where the lateral strains $\varepsilon_{n,t}$ are defined as in (9), and where the coefficient c_ν has the same purpose as in (10) and (13).

In these equations, all the stresses are related to the corresponding strains via (5).

3.2. ***Solution procedure for the case with $\mu > 0$.*** The above equations are used to compute all the Q_i values, half-wave by half-wave, and to obtain the total lateral thrust Q_{TOT} through (2). As done in [Dehghani and Tremblay 2017], the local contact forces Q_i are computed one half-wave at a time, starting from the first one, at the fixed point *FP*. Owing to the assumed symmetry of the problem with respect to the *FP*, only one half of the core is considered, for example the left one, of length $L/2$. The results computed for this left half will be multiplied by 2 to obtain the lateral thrust Q_{TOT} for the full BRB.

The loading, for the problem, is the average global strain ε_0 of (4). A fixed value for the coefficient ξ, among those shown in Figure 2, must be selected.

First half-wave. For the first half-wave, the input term is the average strain ε_A in the top flat portion of Figure 4, uniquely related in a yet unknown way to ε_0. This is given a tentative value $\varepsilon_{1,A}$, and an external iterative loop will be employed to calculate its correct value. In the calculations presented here, this initial value has always been $\varepsilon_{1,A} = \varepsilon_0/2$.

Given a numerical value for $\varepsilon_{1,A}$, the equations presented above allow one to compute all the unknowns in terms of the stress σ_B only. The constitutive law (5) gives the stress σ_A. A tentative value for σ_B is then chosen, and a Newton–Raphson procedure will iterate on it, at each half-wave, to compute its correct value.

Given a tentative value for σ_B, the associated average strain ε_B is given by the inverse of (5). Next, (6) gives $\varepsilon_{B,cic}$, from which, using (6), (7), (10), and (11), one determines the value of $l_{0,1}$ for this half-wave. Equation (20) gives Q_i:

$$Q_i = \frac{\sigma_B A_B^* - \sigma_A A_A^*}{\mu} \tag{26}$$

which holds only if $\mu > 0$. The frictionless case, much easier, will be summarized in the next subsection.

Equation (21) allows one to compute numerically, via the Newton–Raphson technique, the values of both σ_C and ε_C. Next, the values of Δ_i (13), l_B^* (23), and u_B (18) can all be determined from the quantities already computed.

At this point, only the rotation equilibrium equation (22) remains to be satisfied, in the unknown value of σ_B. As said, a Newton–Raphson iterative procedure is adopted to compute the correct value of σ_B. In this procedure, the derivative of (22) with respect to σ_B has to be computed numerically.

Once convergence is reached for σ_B, the values of all the other quantities are also determined, and one can compute the shortening δu_1 of the first half-wave from (15). The length of the first half-wave is obviously $l_{0,1}$.

Generic half-wave. If $l_{0,1}$ is smaller than $L/2$ (otherwise the problem is ill-posed), the next half-wave is taken into account. The following calculations are repeated as many times as necessary, as explained later on.

The input is now the stress σ_A, equal, for equilibrium, to the stress σ_C of the previous half-wave. This is easy to understand, if one considers the next half-wave as the specular, horizontally to the left, of the previous one as shown in Figure 4 (and so on for the subsequent half-waves).

The governing equations are then exploited as before, adopting a new tentative value for σ_B and then iterating on it to satisfy (22), to obtain its correct value. At the end of the calculation, a test on the total length of the solved half-waves must be performed. Call this length L_{comp}, with

$$L_{comp} = \sum_k l_{0,k}, \tag{27}$$

k running from 1 to the number of the current half-wave. If $L_{comp} \le L/2$ then the current half-wave is a "normal" half-wave. Otherwise this half-wave can not be of the computed length l_0, but must be shorter: therefore this is the last half-wave, to be treated in a different way.

If the current half-wave is not the last one, at this point the accumulated horizontal displacement over all the solved half-waves is computed, by adding the contribution of the current half-wave. One moves then on to the next generic half-wave.

If $L_{comp} > L/2$, one ignores the calculations done for this half-wave and goes to the last half-wave.

Last half-wave. We now denote by $l_{0,theor}$ the last half-wave length computed in the previous step, a length which, added to all the previous ones, exceeds the total core length available. The actual length of the last half-wave, according to the check illustrated here above, can be anything from infinitesimal to infinitesimally smaller than $l_{0,theor}$. There is no clear rule to treat this case, and a somewhat arbitrary procedure was followed. We observe that nothing is said, about this point, in [Dehghani and Tremblay 2017].

In the first place, the length of the last half-wave is known from (27), and given by

$$l_{0,last} = L_{comp} - \frac{L}{2} \tag{28}$$

(recall that here $L_{comp} > L/2$). It is then assumed that two possible situations may exist.

If $l_{0,last}$ is smaller than the sum of l_A and l_B associated to $l_{0,theor}$, i.e.,

$$l_{0,last} < \left(\tfrac{1}{2} + \gamma\right) l_{0,theor}, \tag{29}$$

one considers the last wave as a "short" one, flat, with no further contribution to the total thrust Q_{TOT}. Only the total length is updated, and the total shortening, by adding a final value for δu_i which ignores the bending contribution.

If, on the contrary,

$$l_{0,last} \geq \left(\tfrac{1}{2} + \gamma\right) l_{0,theor}, \tag{30}$$

then this wave is treated as a "long" one, with contact points at both the upper and the lower sides of the core, and with known half-wave length (28). The new associated value of ξ is computed from (11) used in an inverse way. This half-wave gives therefore a full contribution to the total thrust, that can now be computed as for any other intermediate wave.

At the end of the solution of this last half-wave, by construction the total accumulated length is equal to $L/2$, and the total horizontal displacement δu is computed by adding the contribution of the last half-wave.

External loop over $\varepsilon_{1,A}$. Recall now that all this procedure starts from a tentative value for the strain $\varepsilon_{1,A}$ in the very first segment of the core, at the *FP*. In general, therefore, even though all the equilibrium equations are satisfied, the computed value of δu will be different from the given value $u_{max}/2$ (recall that the presented calculation holds for one half of the core), associated to the given average strain ε_0. An external iterative loop is therefore implemented which, after each set of calculations, updates the tentative value for $\varepsilon_{1,A}$ in the first half-wave by means of the equation

$$\varepsilon_{1,A}^{new} = \varepsilon_{1,A}^{old} \frac{u_{max}}{2\delta u}. \tag{31}$$

One then restarts from the first half-wave, and proceeds until convergence on ε_A of the first wave is reached, so as to have the correct shortening value at the ends of the core. Unfortunately, there is no guarantee to always obtain this convergence for all the possible choices of ξ. In some cases, especially for the smaller values ($\xi = 1.4303$ and $\xi = 2$), no solution to the problem could be found. It is not easy to tell if this happens because these values for ξ are physically meaningless, for the given set of data, or because the implemented method introduces unrealistic contributions for some values of ξ.

Attention should be paid, in the said calculations, to all the cases in which $\gamma = 0.5$, because these cases, as obvious from Figure 4, correspond to the absence of the flat segments A and C in all the buckled half-waves. The necessary changes in all the equations, however, are trivial.

3.3. ***Solution procedure for the case with*** $\boldsymbol{\mu = 0}$**.** In the frictionless case (26) is no longer valid, obviously. On the other hand, since the average stress and strain are constant all along the BRB core, the situation is much simpler, because now all the half-waves are equal, and have the same value of Q_i,

except the last one. Therefore, given a tentative value for $\varepsilon_{1,A}$ in the first core segment at the *FP*, the only unknown to be computed is the normal contact force Q_i, and (22) is adopted for this calculation. Once again, a Newton–Raphson loop is implemented for solving (22) given a tentative value for Q_i. Once a converged value of Q_i is computed, the corresponding value of l_0 allows one to determine the number of "standard" half-waves (with length l_0) associated to it. From this, one obtains the length of the last half-wave (shorter than l_0), the sum of the normal contact forces, and the accumulated shortening. The last half-wave is treated as in the case with friction, only computing, if necessary, the last contact force Q_i instead of σ_B from (22).

When all the half-waves have been solved, the same iterative procedure on $\varepsilon_{1,A}$ is adopted to obtain convergence also on the given shortening value u_{max}.

4. Total lateral thrust: computed results

The technique illustrated in the previous section was implemented in a Fortran code which requires a fraction of a second to run for a single BRB problem. Reference is first made to the following set of data parameters, which describe one of the reduced-scale, all-steel, bolted BRBs studied in [Metelli et al. 2016]:

- $L = 560\,\text{mm}$, $\varepsilon_0 = 0.02$, $u_{max} = 11.2\,\text{mm}$;
- $b = 50\,\text{mm}$, $t = 5\,\text{mm}$;
- $g = 1\,\text{mm}$;
- $K_{TOT} = 416372\,\text{N/mm}$;
- $E = 150000\,\text{MPa}$, $\nu = 0.33$, $\sigma_0 = 230\,\text{MPa}$, $n = 13$, $\alpha = 0.01$;
- $\mu = 0.15$.

This BRB is expected to furnish a severe test to the adopted algorithm, because of the high gap to section height ratio, close to the limit of its possible practical applicability. This high ratio is associated to a "large" buckled amplitude and to other possible difficulties, both theoretical and practical, as suggested, for example, in [Takeuchi and Wada 2017]. At the same time, however, this BRB is expected to provide a clearer evidence of the difficulties that accompany the calculation of the total lateral thrust Q_{TOT}.

Note that, in this work, no attention is given to the issue of producing engineering interesting results for any BRB type. The only aim is to highlight the really important factors which contribute to the determination of the total lateral thrust.

The first result, shown in Figure 5, is the dependence of Q_{TOT} on the choice of the wavelength parameter ξ, setting equal to 1 all the c_i coefficients of the previous sections. This dependence appears to be the most important among all the considered factors. If one changes the value of ξ, in fact, the computed value of Q_{TOT} can change by a factor of about 2, and the total number of buckled waves (for the full core) N is predicted in a range between $N = 6$ and $N = 10$.

Figure 6 summarizes the importance of the other factors on the computed value of Q_{TOT}. This figure, as well as all the following ones except when explicitly indicated, shows results all obtained with $\xi = 3$, as suggested in previous work [Bregoli et al. 2016].

In Figure 6, the vertical axis shows the value of Q_{TOT} normalized with respect to the "best" one, which considers all the contributions to the adopted equations (leftmost bar, marked by "All", and central bar

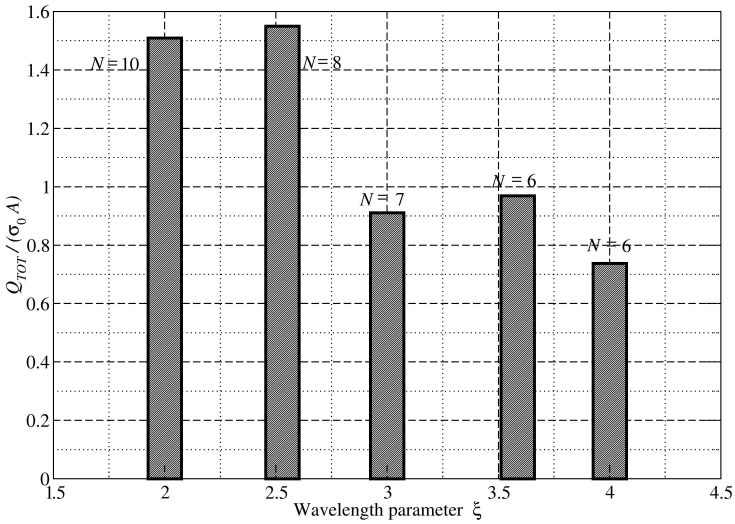

Figure 5. Reduced-scale BRB example. Variation of the total lateral thrust Q_{TOT} with the choice of parameter ξ of (11). N denotes the predicted total number of buckled waves in the BRB. The result for $\xi = 1.4303$ is missing because of lack of convergence.

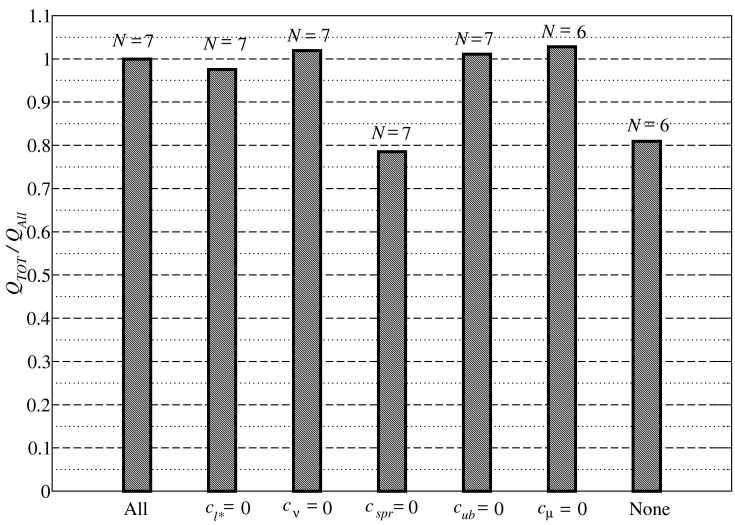

Figure 6. Reduced-scale BRB. Variation of Q_{TOT} associated to different adopted assumptions. Results computed adopting $\xi = 3$. Symbols as explained in the text.

in Figure 5). The second bar, with the $c_{l*} = 0$ label, refers to calculations done neglecting the effect of writing (22) on the deformed configuration for the horizontal length (see (23)). The third bar shows the result which ignores the Poisson and plastic incompressibility effects, i.e., sets $c_\nu = 0$ in (10), (13), and (25). The fourth bar refers to the case of a rigid containment, i.e., $c_{spr} = 0$ in (13). The fifth bar refers to the case in which the bending contribution to the horizontal shortening is neglected in the calculations, by setting $c_{ub} = 0$ in (15) and (23).

The last two bars refer to the frictionless case: the one marked by $c_\mu = 0$ ignores only the friction, keeping in all the other contributions; the last one, marked by "None", sets all the c_i parameters and μ equal to zero.

Now the differences among the computed values of Q_{TOT} appear less important than in the previous figure. Only the assumption of a rigid containment causes a drop of about 20% in the value of Q_{TOT} (fourth and last bar); otherwise the differences are minimal.

The next figures show in more detail the influence of several parameters on 6 output variables for this problem. The output variables are, from left to right and from top to bottom:

- the total thrust Q_{TOT} normalized with respect to the nominal first yield force $\sigma_0 A$;
- the horizontal force in the core at the *FP*, H_{FP}, also normalized with respect to the first yield force (this ratio depends essentially on the hardening properties of the material);
- the ratio between the horizontal force at the ends of the core, H_{END}, and the horizontal force at the *FP* (the higher this ratio the higher is the contribution of the frictional tangential contact forces);
- the ratio between the average strain at the *FP* and the given average strain ε_0 of (4);
- the ratio between the average strain at the ends of the core, ε_{END}, and the average strain at the *FP* (this is also related to the amount of frictional forces existing between core and restraining profiles);
- the ratio between the total bending contribution to the core shortening, $\sum u_B$, and the total shortening u_{max} itself.

Figure 7 shows the influence of the tangential frictional contact forces, which enter the calculations only in (20) and (21). Varying the value of the friction coefficient μ, as done in Figure 7, is the same as considering μ fixed at some value and examining the effect of introducing tangential contact forces smaller than their theoretical maximum, equal to μQ_i at each contact point. Tangential forces smaller than μQ_i may occur if no relative slip occurs between core and restraining profiles.

Figure 7 shows that, for this BRB, and for $\xi = 3$, the effect of increased frictional forces (top left image, solid line) is to reduce Q_{TOT}. In this case, the assumption of a maximum value for the tangential contact forces would be unsafe, even though the variation in Q_{TOT} is not very high. Nevertheless, this effect can be different. For example, selecting $\xi = 4$ in this calculation, an increasing curve for Q_{TOT} is produced (dashed line in the top left image). In this case, the assumption of the maximum value for the contact tangential forces would be to the safe side.

It is difficult to understand from the equations the general trend for this, since in (18) to (25) several terms contain the contact force Q_i, with conflicting effects. The global change in the value of Q_{TOT}, due to a change of the tangential frictional contact forces, however, is here at most of the order of 10%.

Note, however, that larger changes in the value of Q_{TOT} could be predicted if, upon a change of μ, a change would occur in the predicted number of buckled waves, N. With $\xi = 3$ or $\xi = 4$, the number N remains the same for all the considered values of μ ($N = 7$ for $\xi = 3$, and $N = 6$ for $\xi = 4$). But if one adopts $\xi = 2.529$, in this calculation, one obtains $N = 9$ for small values of μ, and $N = 8$ for large values of μ. The corresponding values of Q_{TOT}, much larger than with $\xi = 3$ or $\xi = 4$ because of the larger value of N, have then a maximum change, with μ, of about 35%. The bottom image of Figure 7, solid line, shown this case. Moreover, with $\xi = 2.529$, the trend for Q_{TOT} is first increasing and then decreasing, passing through a discontinuity (just suggested by the numerical results, which do not find

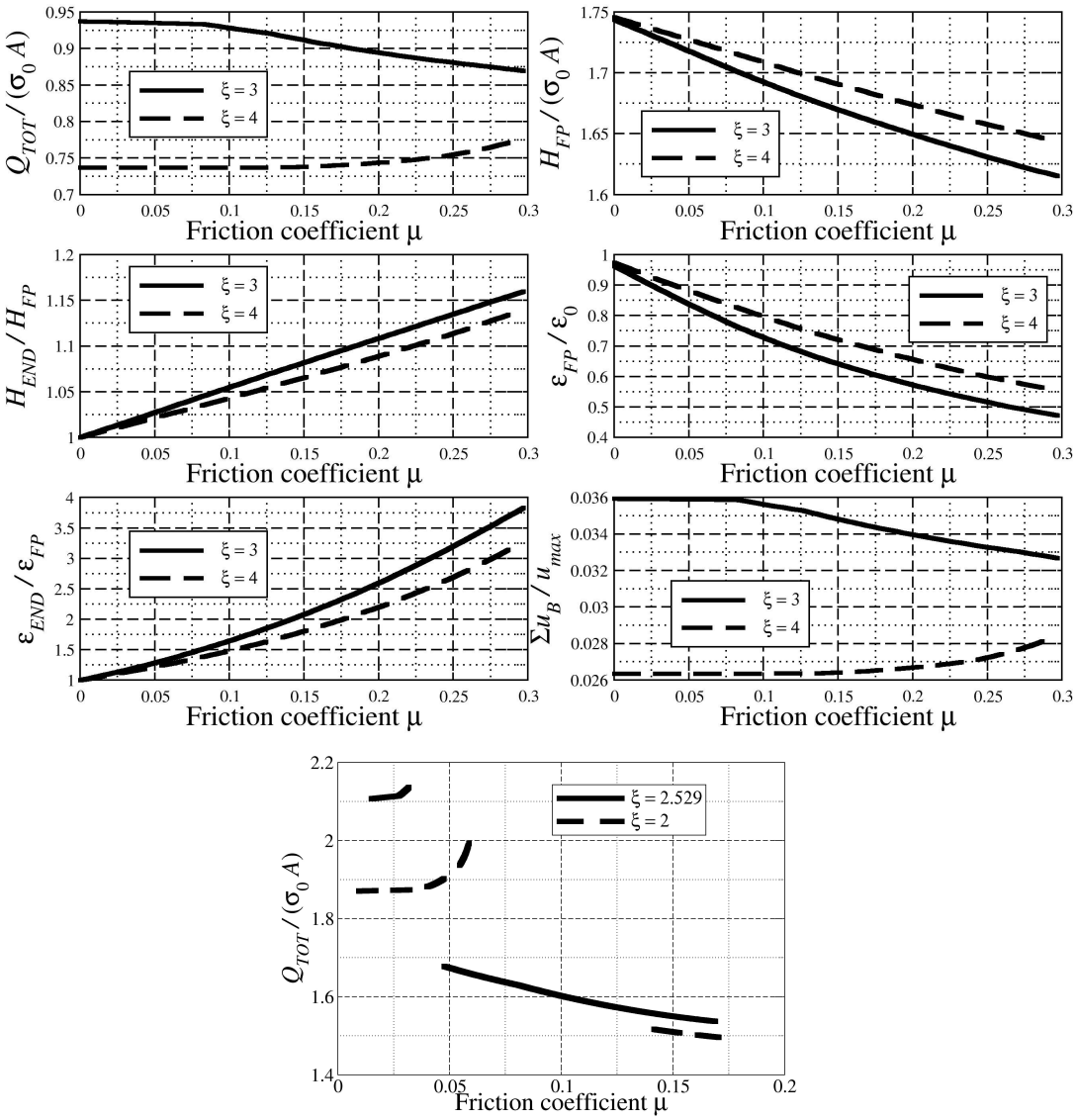

Figure 7. Reduced-scale BRB. Dependence of various mechanical quantities on the friction coefficient μ, with $\xi = 3$ (solid lines) and $\xi = 4$ (dashed lines). The bottom image plots Q_{TOT} computed adopting $\xi = 2.529$ (solid lines) and $\xi = 2$ (dashed lines). Other symbols are explained in the text.

convergence around the discontinuity zone) when N changes. The dashed line in the bottom image of Figure 7 refers to the case with $\xi = 2$, which, despite a large range of values of μ with no convergence, shows more clearly the tendency of Q_{TOT} to jump across some value of μ.

From this image already (but later images will show this more clearly), it appears that the value of Q_{TOT} has a discontinuous dependence on some parameters. This is important to keep in mind, because it is a clear symptom of the difficulty in accurately predicting, by any method, the value of Q_{TOT}.

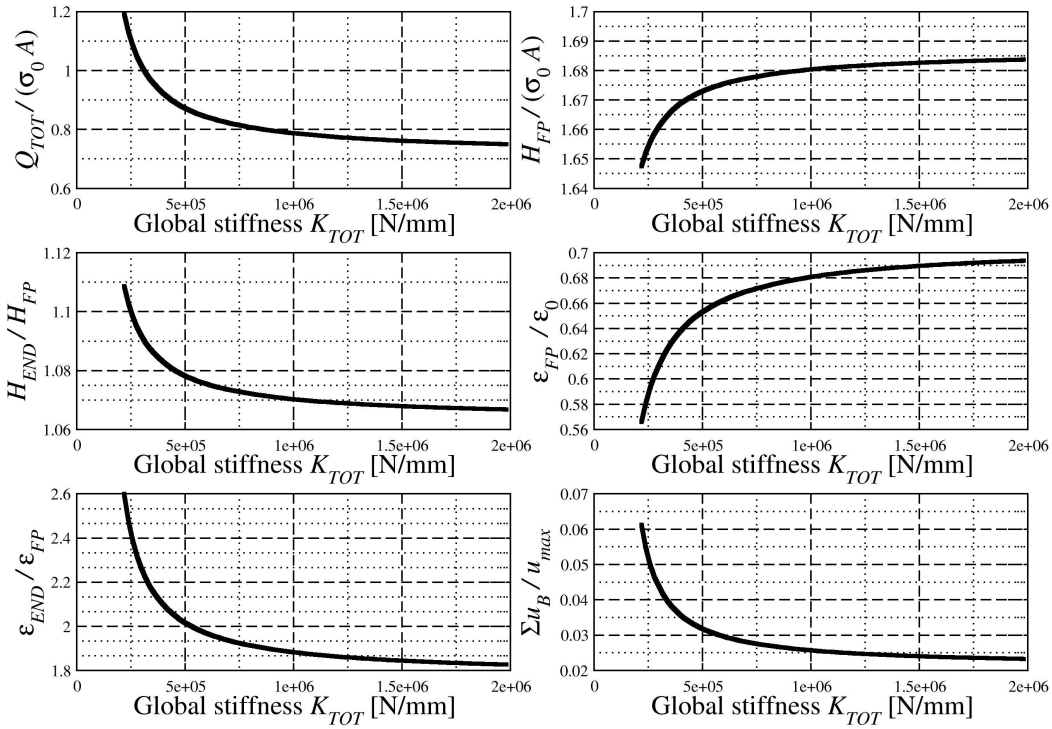

Figure 8. Reduced-scale BRB. Dependence of various mechanical quantities on the restrainer global elastic stiffness K_{TOT}. Results computed adopting $\xi = 3$. Other symbols as explained in the text.

The right bottom image in Figure 7 shows that the contribution obtained by accounting for the bending deflection u_B of (18) is negligible (order of few percents), although for $\xi = 3$ is larger than for $\xi = 4$, and with an opposite trend for increasing μ. This seems reasonable considering that $\xi = 4$ is associated to a shorter inclined portion of the buckled half-waves than $\xi = 3$.

The other images in Figure 7 indicate that some of the plotted variables are sensitive to the value of μ. Nevertheless, with the exception of H_{END}, whose value changes by about 15% in the considered range of values for μ, these variables have little engineering importance.

Figure 8 shows the effect of the global elastic stiffness K_{TOT} of the restraining profiles on the same output quantities. If K_{TOT} becomes small, all the plotted quantities tend to grow (positively or negatively) rapidly. In the frictionless, linear elastic case, Genna and Bregoli [2014] have shown analytically this jump of the total thrust, which can pass through vertical asymptotes (typical of linear elasticity only), for decreasing values of K_{TOT}. If K_{TOT} is too small, moreover, all the values for the ξ coefficients should be reconsidered, since they might be much higher than those adopted here, as shown in [Genna and Bregoli 2014].

Figure 9 refers to the value of the Young modulus E. This influences the reduced modulus E_R which governs the half-wave length through (11), and its effect, on Q_{TOT}, is not negligible at all, while all the other plots do not show anything new. Figure 10 illustrates the effect of varying the yield stress σ_0, a parameter of obvious importance. Once again, a change in σ_0 produces a significant change in Q_{TOT}.

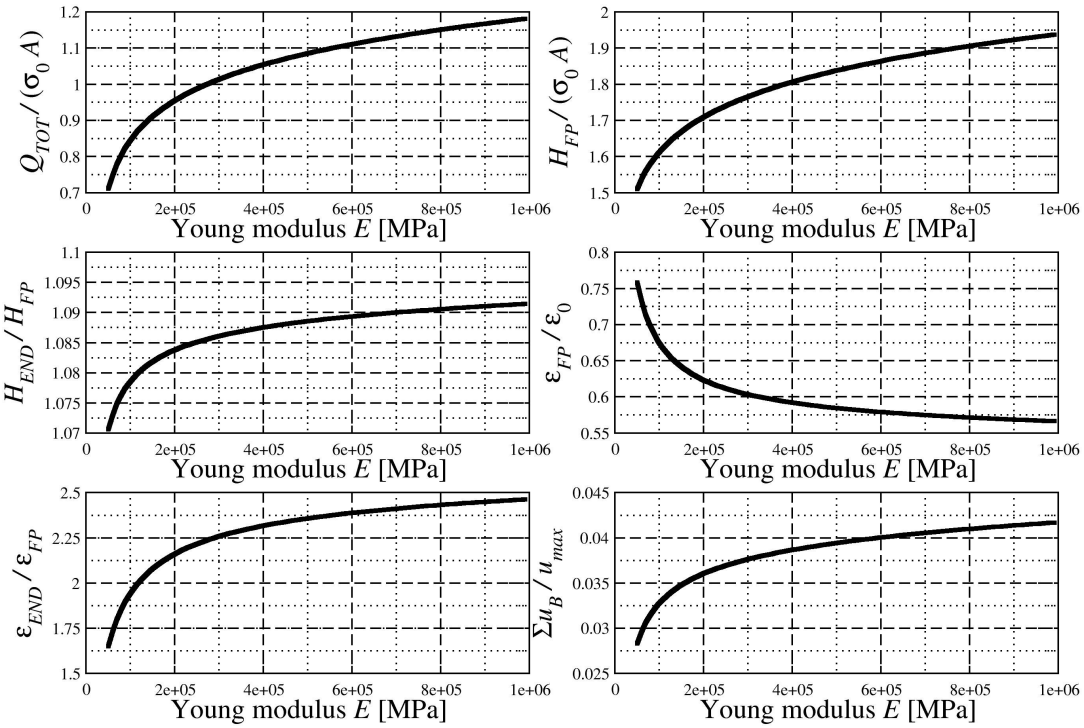

Figure 9. Reduced-scale BRB. Dependence of various mechanical quantities on the core Young modulus E. Results computed adopting $\xi = 3$. Other symbols as explained in the text.

Figure 11 refers to the exponent n of the Ramberg–Osgood equation adopted for the steel constitutive law (5). In this equation, $n = 1$ corresponds to a linear elastic material, and increasing values of n produce a nonlinear hardening that, for $n \to \infty$, tends to perfect plasticity at $\sigma = \sigma_0$. Changing the value of n produces a very large change in Q_{TOT}, with significant discontinuities. These are due to a change in the predicted number of buckled waves associated to the same final core shortening. In all the previous plots (Figures 7 to 10), for $\xi = 3$, the number N of buckled waves was always $N = 7$; here, N goes from $N = 4$ for small values of n to $N = 8$ for large values of n. Correspondingly, Q_{TOT} changes much.

An increase of the exponent n produces also very large values for ε_{END}, since the material stiffness tends then to vanish. Large values of n make the material approach perfect plasticity; this is confirmed also by $H_{FP} \to \sigma_0 A$ in the top right image. In any case, however, the $\sum u_B$ quantity remains negligible.

In general, it can be observed that the definition of the stress-strain law in its entirety plays a very important role in this calculation.

The next two figures are equivalent to Figures 5 and 6, but refer to a different BRB setup, taken from [Dehghani and Tremblay 2017]. Here the design parameters are the following:

- $L = 3000\,\text{mm}$, $\varepsilon_0 = 0.03$, $u_{max} = 90\,\text{mm}$;
- $b = 150\,\text{mm}$, $t = 19.05\,\text{mm}$;
- $g = 0.9\,\text{mm}$;

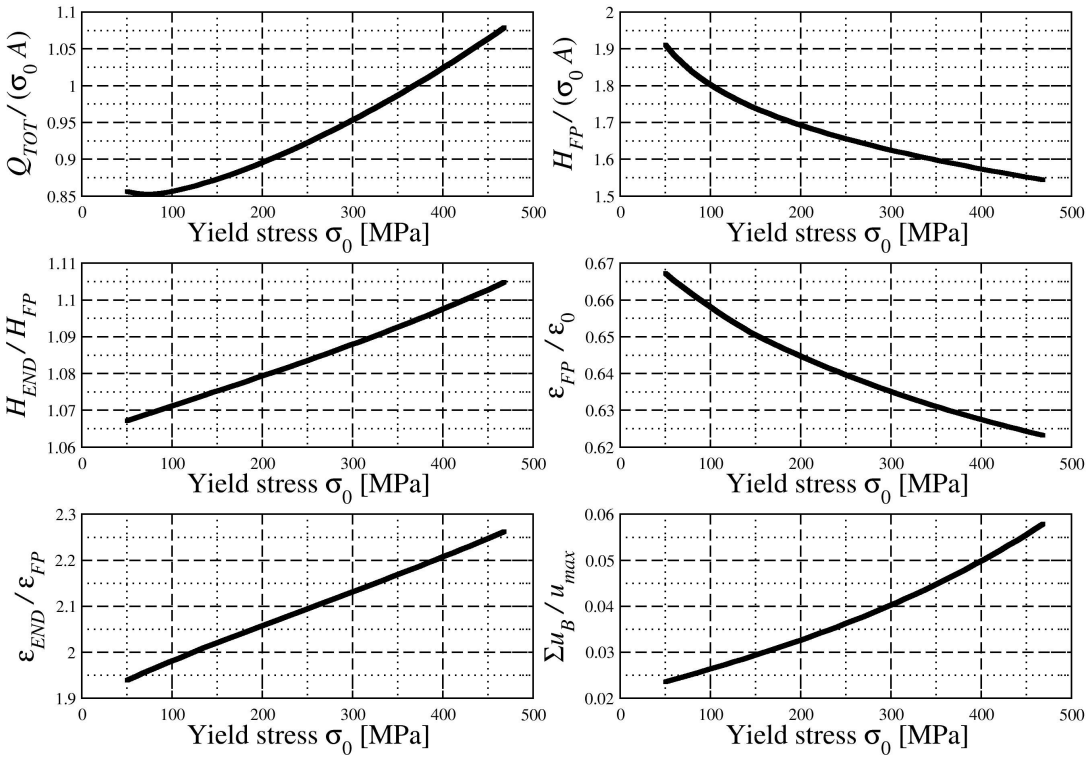

Figure 10. Reduced-scale BRB. Dependence of various mechanical quantities on the core first yield stress σ_0. Results computed adopting $\xi = 3$. Other symbols as explained in the text.

- $K_{TOT} = 2400000\,\mathrm{N/mm}$;
- $E = 150000\,\mathrm{MPa}$, $\nu = 0.33$, $\sigma_0 = 330\,\mathrm{MPa}$, $n = 13$, $\alpha = 0.01$;
- $\mu = 0.15$.

This is a full-scale, all-steel BRB, with a much longer dissipative core length L, a much bigger cross-section of the core, a much higher restrainer stiffness, but a smaller total gap g than the one considered in the first example. The smallness of this gap is expected to reduce much, in proportion, both the amplitude of the buckled bending deflections and the total lateral thrust. This choice may be closer to those adopted in engineering practice; it has a possible drawback in the possibility that the lateral expansion of the core, under compression, might cause the core itself to get stuck against the retention profiles. A check for this occurrence has been coded into the implemented software, but in all the examples tested, for "reasonable" values of ε_0, no such problem ever occurred.

Figure 12 shows the dependence of Q_{TOT} on the choice of ξ. As in Figure 5, this variation can be of the order of 100%, and the change of the wave number N is also very significant.

Figure 13 illustrates the dependence of Q_{TOT} on several other parameters, as described for Figure 6. Here the strong dependence on c_ν stands out, while all the other factors seem to follow the same tendency as for the reduced-scale BRB of Figure 6. If one sets $c_\nu = 0$ in the adopted equations, thus ignoring the

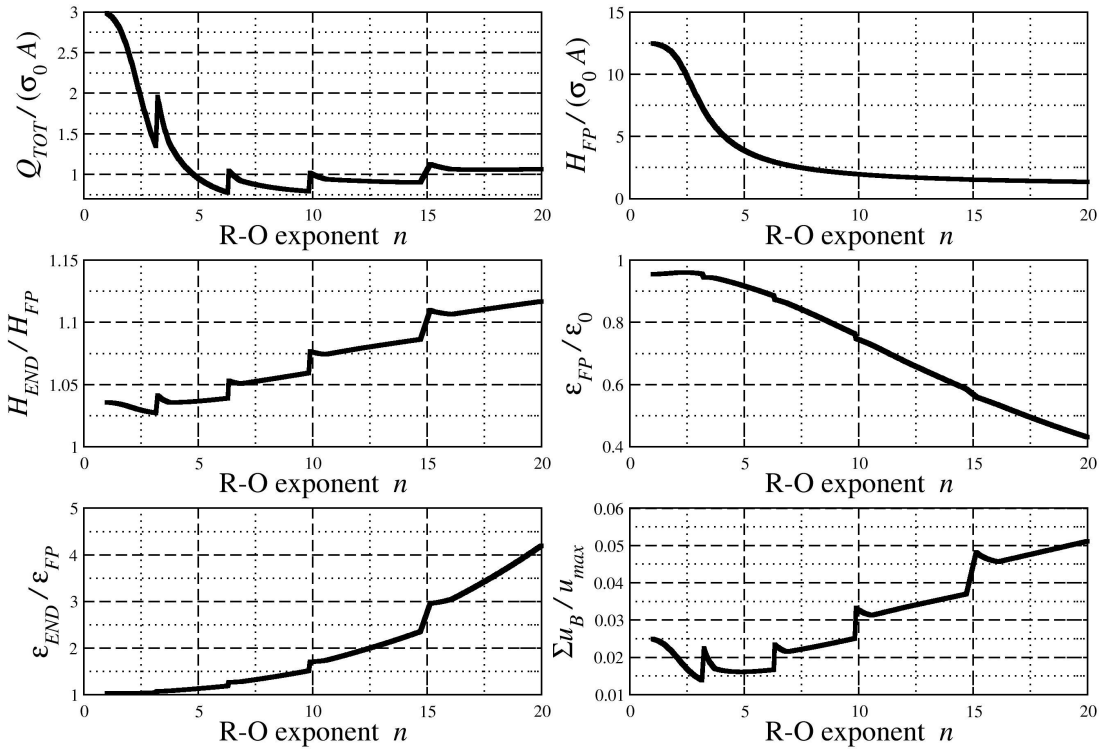

Figure 11. Reduced-scale BRB. Dependence of various mechanical quantities on the Ramberg–Osgood exponent n (5). Results computed adopting $\xi = 3$. Other symbols as explained in the text. The jumps are due to a predicted change in the number N of buckled waves.

contribution of both the Poisson effect and the plastic incompressibility, one obtains a Q_{TOT} value higher by 60% than the "best" one, of the leftmost bar. This effect is due in part to the higher value of the prescribed average strain, here equal to $\varepsilon_0 = 0.03$ instead of $\varepsilon_0 = 0.02$ of the previous case. If one sets $\varepsilon_0 = 0.02$ for this full-scale BRB, one obtains a ratio, between Q_{TOT} with $c_\nu = 0$ and Q_{TOT} with $c_\nu = 1$, equal to 1.22, smaller than the 1.6 shown in Figure 13, yet nonnegligible. The much smaller gap to core thickness ratio, in this last BRB, and the much longer buckled wavelength, might also play a role.

The main reason for this difference, however, is once again that, setting $c_\nu = 0$ for this BRB, the number N of predicted buckled waves increases by one with respect to the case with $c_\nu = 1$. In the case of the reduced-scale BRB of Figure 6, the number N remained the same with $c_\nu = 1$ or $c_\nu = 0$, and the corresponding value of Q_{TOT} did not change much.

Figure 14 illustrates the dependence of the normalized value of Q_{TOT} on the same parameters considered in Figures 7 to 12. In addition, the dependence of Q_{TOT} on μ is plotted for several values of ξ in the bottom right image. The sensitivity to μ is now much lower — almost absent, in fact — than for the reduced-scale BRB, and of a different type, since Q_{TOT} has a maximum for some value of μ. A clear jump of Q_{TOT} across some value of E appears in the left center image, and the same sequence of jumps

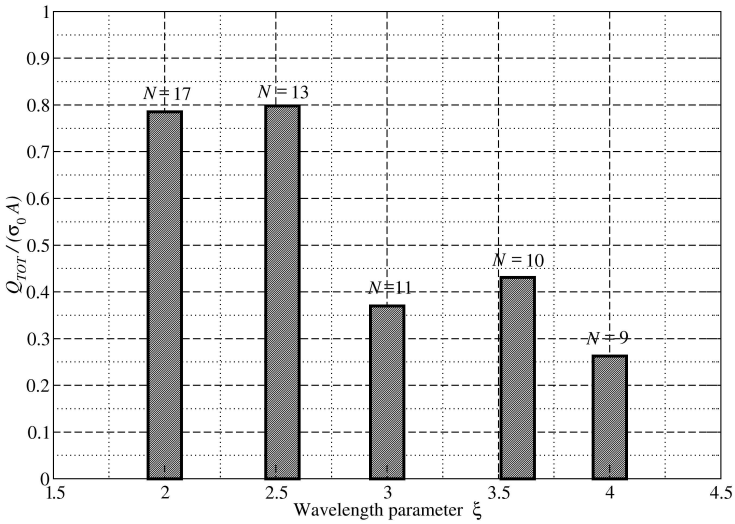

Figure 12. Full-scale BRB example. Variation of the total lateral thrust Q_{TOT} with the choice of parameter ξ of (11). N denotes the predicted total number of buckled waves in the BRB. The result for $\xi = 1.4303$ is missing because of lack of convergence.

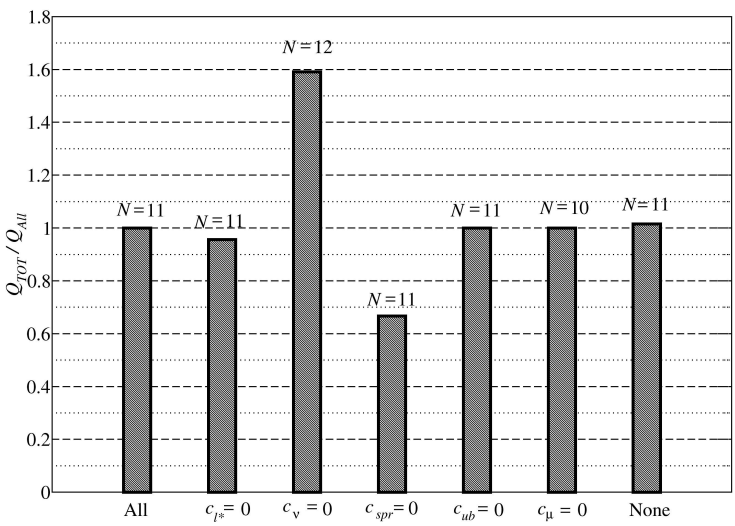

Figure 13. Full-scale BRB. Variation of Q_{TOT} associated to different adopted assumptions. Results computed adopting $\xi = 3$. Symbols as explained in the text.

of Figure 11 is shown in relation to changing n. The relative smallness of the gap g makes almost absent the contribution of $\sum u_B$ to the core shortening (not shown in this figure).

This full-scale BRB, with a proportionally much smaller gap than the reduced-scale one, is "easier" to be solved by means of the adopted scheme, since a failure of convergence did seldom occur. Nevertheless, the strong uncertainties related to the calculation of Q_{TOT} remain unaltered.

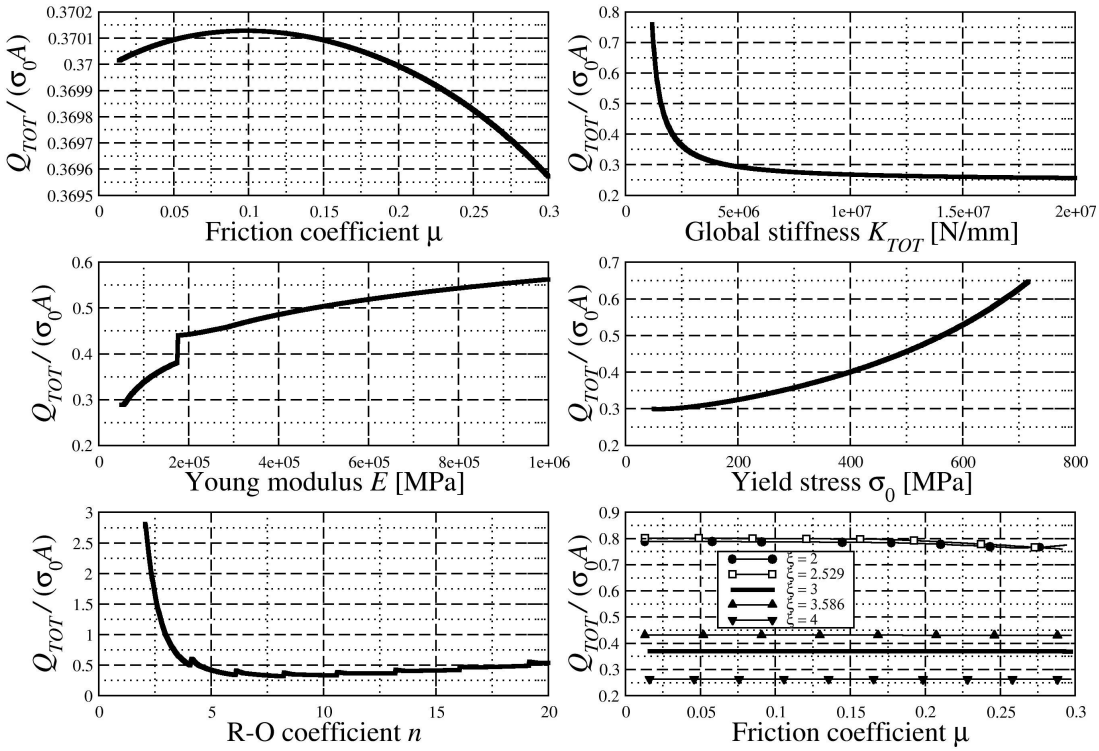

Figure 14. Full-scale BRB. Variation of Q_{TOT} associated to the variation of several analysis parameters. Results obtained with $\xi = 3$ except in the bottom right image. Symbols as explained in the text.

5. Conclusions

The analytical technique illustrated in this work has been developed firstly as an improvement (and a clarification/correction) of a similar one proposed in [Dehghani and Tremblay 2017], secondly as a tool to understand what factors do matter in the calculation of the total lateral thrust Q_{TOT} in BRBs.

The calculations illustrated in this work allow one to conclude what follows, with reference to the calculation of Q_{TOT}.

- The main factor, in this problem, is the number N of waves developed by the BRB buckled core, associated to the value of the parameter ξ of (11). It was shown that a change of ξ produces the largest changes in the lateral thrust Q_{TOT}. Unfortunately, there is no theoretical basis allowing an engineer to select the "correct" value for ξ, among the various equally possible.
- A correct estimate of the stiffness of the restraining profiles is crucial as well. Quite possibly (this was not investigated, here), also the local details of such stiffness may have a high importance.
- A good set of material data for the stress-strain law is also important, including details about the hardening properties under cyclic loading.

- The effect of the tangential frictional contact forces does not seem to be as important as the previous factors. At the light of the uncertainties introduced by the difficulty in selecting ξ, K_{TOT}, and the material parameters, it seems that one may ignore, or treat in the simplest possible way, the contribution due to the friction.
- The lateral expansion of the core can be important, but also this effect appears of a smaller order of magnitude, compared with the first ones.
- Details such as the distinction between l_B and l_B^* in (22), and others discussed above, do not seem to matter, and the simplest calculations could be adopted without a significant loss of accuracy.

It should be kept in mind that Q_{TOT} depends on almost every parameter in a discontinuous way. Therefore, even its limiting — lower and upper — values may be very wrong, if the set of calculation details, including all the data, happens to be defined in the proximity of a jump in the value of Q_{TOT}.

Another very important effect has been ignored in these calculations, as well as in all the ones proposed in the literature. This is the progressive strong increase of Q_{TOT} with the number of loading cycles, even of the same peak amplitude. It is obvious that a correct analytical tool should somehow incorporate also this effect; to the best of this author's knowledge, unfortunately, there is no available theory about this aspect, which might deserve future attention.

When dealing with BRBs, in conclusion, one should always be aware of the uncertainty associated to the calculation of the buckled wavelength, of the discontinuous dependence of Q_{TOT} on the model details, and of the current lack of knowledge about the dependence of Q_{TOT} on the number of loading cycles.

If one is ready to accept these limitations, it seems that a reasonable compromise, for the calculation of Q_{TOT}, might consist in (i) the adoption of a global method, without proceeding one half-wave at a time; (ii) accounting for friction in some simple approximate way, as was done for example in [Bregoli et al. 2016]; (iii) limiting oneself to computing extreme — minimum and maximum — values for Q_{TOT}. Accepting such a procedure, one should then check the lack of discontinuities in the proximity of these extremes for Q_{TOT} (a tedious procedure, obviously), and finally somehow select a statistically significant value to be adopted for the proper design of the BRB restraining profiles and details.

In this author's opinion, in view of much accumulated evidence, BRBs are structural elements whose design has not yet reached a sufficiently acceptable basis. Until, and if ever, a complete understanding of the difficult phenomena involved will be acquired, much attention should be paid in the practical usage of BRBs.

Acknowledgments

This work was done within a research project financed by the Italian Ministry of Education and Research (MIUR).

References

[Bažant and Cedolin 1991] Z. P. Bažant and L. Cedolin, *Stability of structures: elastic, inelastic, fracture and damage theories*, Oxford Engineering Science Series **26**, Oxford University, New York, 1991.

[Bregoli et al. 2016] G. Bregoli, F. Genna, and G. Metelli, "Analytical estimates for the lateral thrust in bolted steel buckling-restrained braces", *J. Mech. Mater. Struct.* **11**:2 (2016), 173–196.

[Dehghani and Tremblay 2017] M. Dehghani and R. Tremblay, "An analytical model for estimating restrainer design forces in bolted buckling-restrained braces", *J. Constr. Steel Res.* **138** (2017), 608–620.

[Dehghani and Tremblay 2018] M. Dehghani and R. Tremblay, "Design and full-scale experimental evaluation of a seismically endurant steel buckling-restrained brace system", *Earthq. Eng. Struct. Dyn.* **47**:1 (2018), 105–129.

[Genna 2019] F. Genna, "On the sensitivity of Finite Element results in the calculation of the lateral thrust for all-steel buckling-restrained braces", *Eng. Struct.* **194** (2019), 66–76.

[Genna 2020] F. Genna, "Lateral thrust in all-steel buckling-restrained braces: experimental and FEM results", *Eng. Struct.* **213** (2020), art. id. 110512.

[Genna and Bregoli 2014] F. Genna and G. Bregoli, "Small amplitude elastic buckling of a beam under monotonic axial loading, with frictionless contact against movable rigid surfaces", *J. Mech. Mater. Struct.* **9**:4 (2014), 441–463.

[Genna and Gelfi 2012] F. Genna and P. Gelfi, "Analysis of the lateral thrust in bolted steel buckling-restrained braces, I: Experimental and numerical results", *J. Struct. Eng.* (*ASCE*) **138**:10 (2012), 1231–1243.

[Jiang et al. 2015] Z. Jiang, Y. Guo, B. Zhang, and X. Zhang, "Influence of design parameters of buckling-restrained brace on its performance", *J. Constr. Steel Res.* **105** (2015), 139–150.

[Metelli et al. 2016] G. Metelli, G. Bregoli, and F. Genna, "Experimental study on the lateral thrust generated by core buckling in bolted-BRBs", *J. Constr. Steel Res.* **122** (2016), 409–420.

[Ramberg and Osgood 1943] W. Ramberg and W. R. Osgood, "Description of stress-strain curves by three parameters", tech. note 902, National Advisory Committee For Aeronautics, Washington, DC, 1943, Available at http://hdl.handle.net/2060/19930081614.

[Takeuchi and Wada 2017] T. Takeuchi and A. Wada (editors), *Buckling-restrained braces and applications*, Japan Society of Seismic Isolation, Tokyo, 2017.

Received 16 Mar 2020. Accepted 29 Apr 2020.

FRANCESCO GENNA: francesco.genna@unibs.it
Department of Civil Engineering, University of Brescia, Brescia, Italy

JOURNAL OF MECHANICS OF MATERIALS AND STRUCTURES

msp.org/jomms

Founded by Charles R. Steele and Marie-Louise Steele

See msp.org/jomms for submission guidelines.

JoMMS (ISSN 1559-3959) at Mathematical Sciences Publishers, 798 Evans Hall #6840, c/o University of California, Berkeley, CA 94720-3840, is published in 10 issues a year. The subscription price for 2020 is US $660/year for the electronic version, and $830/year (+$60, if shipping outside the US) for print and electronic. Subscriptions, requests for back issues, and changes of address should be sent to MSP.

JoMMS peer-review and production is managed by EditFLOW® from Mathematical Sciences Publishers.

PUBLISHED BY

mathematical sciences publishers

nonprofit scientific publishing

http://msp.org/

Journal of Mechanics of Materials and Structures

Volume 15, No. 3 May 2020